Crystal structure of the thioesterification conformation of *Bacillus subtilis o*-succinylbenzoyl-CoA synthetase reveals a distinct substrate-binding mode

Received for publication, April 7, 2017, and in revised form, May 25, 2017 Published, Papers in Press, May 30, 2017, DOI 10.1074/jbc.M117.790410

Yaozong Chen[‡], **Tin Lok Li**[‡], **Xingbang Lin**[‡], **Xin Li**[§], **Xiang David Li**[§], **and Zhihong Guo**[‡1]

From the [‡]*Department of Chemistry, Hong Kong University of Science and Technology, Clear Water Bay, Kowloon, Hong Kong and the* [§]*Department of Chemistry, University of Hong Kong, Pokfulam, Hong Kong, China*

Edited by Wolfgang Peti

o-Succinylbenzoyl-CoA (OSB-CoA) synthetase (MenE) is an essential enzyme in bacterial vitamin K biosynthesis and an important target in the development of new antibiotics. It is a member of the adenylating enzymes (ANL) family, which reconfigure their active site in two different active conformations, one for the adenylation half-reaction and the other for a thioesterification half-reaction, in a domain-alternation catalytic mechanism. Although several aspects of the adenylating mechanism in MenE have recently been uncovered, its thioesterification conformation remains elusive. Here, using a catalytically competent *Bacillus subtilis* mutant protein complexed with an OSB-CoA analogue, we determined MenE high-resolution structures to 1.76 and 1.90 Å resolution in a thioester-forming conformation. By comparison with the adenylation conformation, we found that MenE's C-domain rotates around the Ser-384 hinge by 139.5° during domain-alternation catalysis. The structures also revealed a thioesterification active site specifically conserved among MenE orthologues and a substrate-binding mode distinct from those of many other acyl/aryl-CoA synthetases. Of note, using site-directed mutagenesis, we identified several residues that specifically contribute to the thioesterification half-reaction without affecting the adenylation half-reaction. Moreover, we observed a substantial movement of the activated succinyl group in the thioesterification half-reaction. These findings provide new insights into the domain-alternation catalysis of a bacterial enzyme essential for vitamin K biosynthesis and of its adenylating homologues in the ANL enzyme family.

o-Succinylbenzoyl-CoA (OSB-CoA)[2] synthetase (MenE) is an essential enzyme in the menaquinone biosynthesis (1–3), which operates only in microorganisms and is an attractive target for development of novel antibiotics (4–6). It catalyzes ATP-dependent activation of *o*-succinylbenzoic acid (OSB) like other acyl-CoA synthetases (Fig. 1) and is an adenylating enzyme of the ANL family (7), which encompasses acyl/aryl-CoA synthetases (ACS), adenylation domains of non-ribosomal peptide synthetases, and firefly luciferases. The adenylating enzymes in the ANL family are highly diverse with low sequence homology (~20% identity), and their representatives have been found to reconfigure their active site in two different active conformations, one for the adenylation half-reaction and the other for the thioesterification half-reaction, in a domain-alternation catalytic mechanism (7). Formation of the two active conformations involve rotation of the small C-terminal domain (C-domain) relative to the large N-terminal domain (N-domain) by a large angle, as much as 140° as observed for bacterial acetyl-CoA synthetase (8) and 4-chlorobenzoate: coenzyme A ligase (4CBL) (9). Supporting evidence for this catalytic mechanism has been accumulated in the last 2 decades (10–13), and a few ANL members have been structurally characterized for both active conformations (9, 14–20).

Because of its medicinal value as an antibiotic target, MenE has been scrutinized for its catalytic mechanism using kinetic and structural methods (5, 21). Consistent with its expected use of the domain-alternation catalytic strategy, *Bacillus anthracis* MenE has been kinetically analyzed to adopt an ordered Bi Uni Uni Bi Ping-Pong catalytic mechanism in which the enzyme sequentially binds ATP and OSB (Bi), releases pyrophosphate (Uni) after adenylation, binds CoA (Uni) as the third substrate, and then releases OSB-CoA and AMP (Bi) after thioesterification (22). Using crystallographic methods, ligand-free MenE orthologues from various sources have been shown to adopt an open conformation with their C-domains rotated at a widely variable angle relative to the N-domains (PDB code 3ipl) (23, 24), which is closed by binding of ATP through an open-closed conformational change to form the compact conformation for the first half-adenylation reaction as captured in the crystal structure of *Bacillus subtilis* MenE (*bs*MenE) in complex with ATP (24). The *bs*MenE-ATP structure confirms the role of transition state stabilization for a strictly conserved lysine residue (Lys-471 in *bs*MenE) and reveals the structural details of

This work was supported by Grants GRF601413 and N_HKUST621/13 (to Z. G), and Grants CRF C7029-15G and AoE/P-705/16 (to X. D. L) from the Research Grants Council of the Government of HKSAR. The authors declare that they have no conflicts of interest with the contents of this article.
The atomic coordinates and structure factors (codes 5X8F and 5X8G) have been deposited in the Protein Data Bank (http://wwpdb.org/).

[1] To whom correspondence should be addressed. Tel.: 852-23587352; Fax: 852-23581594; E-mail: chguo@ust.hk.

[2] The abbreviations used are: OSB-CoA, *o*-succinylbenzoyl-CoA; OSB, *o*-succinylbenzoate; OSB-NCoA, *o*-succinylbenzoyl-amino coenzyme A; OSB-AMP, *o*-succinylbenzoyl-adenosine monophosphate; 4CBL, 4-chlorobenzoate:CoA ligase; ANL enzymes, acyl/aryl-CoA synthetases, adenylation domains of non-ribosomal peptide synthetases and firefly luciferases; r.m.s.d., root-mean-square deviation; PDB, Protein Data Bank; ACS, acyl/aryl-CoA synthetase; IPP, inorganic pyrophosphatase; PNP, purine nucleoside phosphorylase; MESG, 2-amino-6-mercapto-7-methylpurine ribonucleoside; MR, molecular replacement; DHNA, 1,4-dihydroxy-2-naphthoyl-CoA.

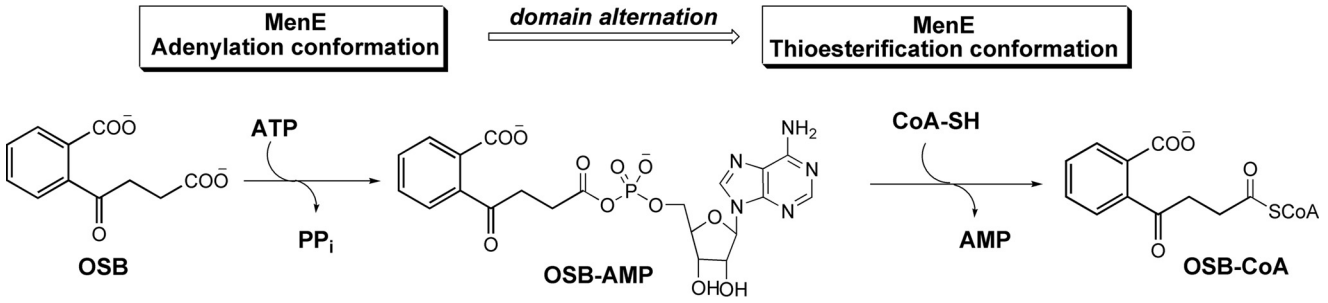

Figure 1. Catalysis of a two-step reaction by OSB-CoA synthetase (MenE) in two distinct active conformations. *PP_i,* pyrophosphate; *CoA–SH,* coenzyme A.

the carboxylate-binding site created by ATP binding. In addition, this structure shows that the strongest interaction between N- and C-domains occurs at the β-phosphate in the triphosphate moiety of ATP to allow easy disassembly of the compact adenylation conformation in an encrypted C-domain release mechanism, which is required after adenylation to allow transition to the thioester-forming conformation in the domain-alternation mechanism. Importantly, this complex structure solidifies a general mode of gripping interactions between the P-loop of ANL enzymes with ATP, which forms the basis for the critical structural role of ATP in configuring the adenylation-active conformation (24).

More recently, we have solved a new *bs*MenE structure in complex with the *o*-succinylbenzoyl-adenosine monophosphate (OSB-AMP) (26), which is subtly different from a previously determined one, also in complex with OSB-AMP (23). This new structure represents the state of the enzyme with the intermediate in a strained conformation formed right after adenylation and provides direct evidence for the in-line backside nucleophilic attack mechanism for the adenylation half-reaction by comparison with the pre-adenylation *bs*MenE-ATP structure (24). Structural comparison also revealed structural changes in both the reactants and the active site that contribute to catalysis of the adenylation reaction. Moreover, with the help of site-directed mutagenesis and kinetic analysis, the conserved His-196 was found to likely desolvate the adenylation active site instead of stabilizing the adenylation transition state. Furthermore, comparison of the new structure with the previous OSB-AMP-bound structure allows us to propose a mechanism of the post-adenylation C-domain release, which may be driven by the relaxation of the strained succinyl group from an *eclipsed-* to *anti*-conformation. These results not only allow us to better understand the adenylation reaction mechanism, but also provide clues on how the enzyme changes from its active adenylation conformation to the thioesterification conformation in the domain-alternation mechanism.

To further understand the MenE catalytic mechanism, it is important to know the structure of the active thioesterification conformation. However, this thioesterification conformation remains elusive despite a previous attempt to determine its atomic structure (23). In this study, we synthesized a non-hydrolyzable analogue of the OSB-CoA product, *o*-succinylbenzoyl-amino coenzyme A (OSB-NCoA), in an attempt to trap the enzyme in the second active conformation. Co-crystallization of the product analogue with the enzyme was successful, but the resulting crystals gave rise to uninterpretable diffraction patterns. To overcome this problem, two non-conserved residues were mutated to obtain a catalytically active variant I454R/A456K (IRAK) and successfully co-crystallized with OSB-NCoA with or without AMP for determination of the targeted thioesterification conformation structure at 1.76 and 1.90 Å resolution, respectively. These structures reveal the unique thioesterification active site of the adenylating enzyme and provide fresh insights into its domain-alternation catalysis.

Results

Crystallization

To capture *bs*MenE in a thioesterification state, we synthesized a non-hydrolyzable analogue of the OSB-CoA product, *o*-succinylbenzoyl-amino coenzyme A (OSB-NCoA), following a reported chemoenzymatic method (27) and used it to co-crystallize with the wild-type enzyme. The co-crystallization was successful, affording large crystals that diffracted to ~1.7 Å in in-house tests. However, most of the reflection spots, either at high or low diffraction angles, suffered severe twinning, which led to uninterpretable data sets. This diffraction problem was not overcome by optimizing the cryoprotectant or the crystallization conditions but was probably due to the intrinsic disorder of the protein complex. Suspecting that this disorder may be caused by loose ligand binding, two non-conserved residues Ile-454 and Ala-456 were mutated into arginine and lysine, respectively, to make a double mutant IRAK (I454R/A456K) to strengthen the binding between OSB-NCoA and the enzyme. This was based on the fact that these two residues correspond to Arg-475 and Lys-477, respectively, of 4CBL in sequence alignment, which form hydrogen bonding or ionic interaction with the adenine ring and 3′-phosphate of the enzyme-bound product analogue 4-chlorobenzoyl-CoA (9). As shown in Table 1, the catalytic efficiency (k_{cat}/K_m) of the double mutant is moderately decreased by 15–26-fold toward ATP or CoA but remains essentially unchanged toward the OSB substrate. In comparison, the single mutant I454R exhibits a very similar level of activity changes as the double mutant, indicating that the other mutation A456K has a negligible effect on catalytic function. The activity results clearly showed that the double mutant is fully competent in catalysis without changing the catalytic mechanism.

Co-crystallization of the IRAK double mutant with OSB-CoA in the presence or absence of AMP was very successful,

Table 1
Single substrate kinetic parameters of wild type *bs*MenE and its mutants

Protein	Substrate	k_{cat}	k_{cat}(WT)/k_{cat}	K_m	K_m/K_m(WT)	k_{cat}/K_m	-Fold decrease in k_{cat}/K_m
		min^{-1}		μ_M		$_M{\cdot}min^{-1}$	
WT	OSB	$(7.2 \pm 0.3) \times 10^2$		44 ± 19		$(1.6 \pm 0.6) \times 10^7$	
	ATP	$(6.3 \pm 0.2) \times 10^2$		24 ± 4		$(2.7 \pm 0.4) \times 10^7$	
	CoA	$(7.3 \pm 0.8) \times 10^2$		$(2.4 \pm 0.8) \times 10^2$		$(3.0 \pm 0.6) \times 10^6$	
I454R	OSB	93 ± 5	7.7	8.6 ± 2.4	0.19	$(1.1 \pm 0.1) \times 10^7$	1.5
	ATP	86 ± 7	3.9	66 ± 21	2.7	$(1.3 \pm 0.4) \times 10^6$	20
	CoA	$(1.6 \pm 0.3) \times 10^2$	4.6	$(1.5 \pm 0.8) \times 10^3$	6.25	$(1.1 \pm 0.5) \times 10^5$	26
I454R/A456K	OSB	95 ± 3	7.6	9.7 ± 1.8	0.22	$(9.7 \pm 1.7) \times 10^6$	1.7
	ATP	$(1.0 \pm 0.1) \times 10^2$	6.3	87 ± 33	3.6	$(1.2 \pm 0.3) \times 10^6$	23
	CoA	$(1.5 \pm 0.1) \times 10^2$	4.9	$(7.6 \pm 0.9) \times 10^2$	3.2	$(2.0 \pm 0.4) \times 10^5$	15
S198A	OSB	$(1.6 \pm 0.1) \times 10^2$	4.5	4.4 ± 0.5	1.1	$(3.6 \pm 0.2) \times 10^7$	0.5
	ATP	$(1.7 \pm 0.1) \times 10^2$	3.7	41 ± 9	1.6	$(4.0 \pm 0.2) \times 10^6$	6.6
	CoA	$(1.6 \pm 0.1) \times 10^2$	4.6	58 ± 17	2.2	$(2.7 \pm 0.8) \times 10^6$	1.1
S384P				No activity			
E392A	OSB	8.8 ± 1.0	82	47 ± 24	1.1	$(1.9 \pm 0.8) \times 10^5$	86
	ATP	10 ± 1	63	39 ± 3	1.6	$(2.6 \pm 0.2) \times 10^5$	104
	CoA	12 ± 3	66	$(5.3 \pm 1.8) \times 10^2$	2.2	$(2.2 \pm 0.2) \times 10^3$	1.3×10^3
S389A	OSB	$(2.4 \pm 0.3) \times 10^2$	3.0	31 ± 12	0.7	$(7.7 \pm 1.8) \times 10^6$	2.1
	ATP	$(2.4 \pm 0.5) \times 10^2$	2.6	39 ± 8	1.6	$(6.1 \pm 1.1) \times 10^6$	4.3
	CoA	$(2.6 \pm 1.1) \times 10^2$	2.8	$(1.2 \pm 0.3) \times 10^3$	5.0	$(2.1 \pm 0.6) \times 10^5$	14
W422A				No activity			
Y452A				No activity			

affording large cubic single crystals. These single crystals diffracted to high resolution without the twinning problem observed for the wild-type enzyme and were used to determine the structures of the binary complex (IRAK–OSB-NCoA) and the ternary complex (IRAK–OSB-NCoA–AMP) at a resolution of 1.90 and 1.76 Å, respectively, by molecular replacement using the N-domain of ligand-free *bs*MenE (PDB code 5BUQ) (24) as the template. The statistics of data collection, data processing, and structural refinement are summarized in Table 2. In a quick examination of the structures, the mutated residues were found to locate on the protein surface at a far distance from the ligand without forming the anticipated interactions or other interactions with other amino acid residues. The improved crystallization properties of the double mutant may be a result of the improved hydrophilicity of the protein surface caused by the mutations.

Table 2
Data collection and refinement statistics

	IRAK–OSB-NCoA–AMP	IRAK–OSB-NCoA
PDB code	5X8F	5X8G
Data collection		
Wavelength (Å)	0.979	0.979
Space group	*P*1	*P*1
Unit cell		
a, *b*, *c* (Å)	71.87, 96.36, 98.07	71.95, 96.48, 97.66
α, β, γ (°)	80.44, 77.96, 81.11	80.14, 77.81, 81.17
Reflections[a]	900,447 (230,857)	892,667 (181,119)
Multiplicity[a]	3.9 (3.9)	4.9 (4.8)
Completeness (%)[a]	92.9 (90.8)	91.5 (92.8)
I/σ_I	10.5 (1.9)	8.5 (2.4)
R_{merge}[a]	0.062 (0.431)	0.114 (0.726)
$CC_{1/2}$[a]	0.997 (0.827)	0.991 (0.811)
Matthews coefficient	2.95	2.95
Structural refinement		
Resolution range (Å)[a]	29.96–1.76 (1.83–1.76)	31.03–1.90 (1.97–1.90)
R_{free}/R_{work} (%)	19.41/16.35	20.60/16.48
No. of non-hydrogen atoms	17,221	16,831
Macromolecules	14,825	14,829
Solvent	2037	1707
Ligands/ions	364	323
Average B-factor (Å^2)[b]		
Macromolecules	27.51	30.98
Ligands	32.15	32.36
Solvent	43.80	39.36
r.m.s.d. for ideal value in		
Bond length (Å)	0.006	0.008
Bond angles (°)	0.87	0.88
Ramachandran statistics (%)[c]	98.0/1.8/0.2	98.0/1.8/0.2

[a] Statistics for the highest-resolution shell are shown in parentheses.
[b] The B-factor values of both structures were calculated from the chain C of the IRAK–OSB-NCoA–AMP structure and the chain D of the IRAK–OSB-NCoA structure.
[c] Ramachandran statistics indicate the fraction of residues in the most favored, allowed, and disallowed regions of the Ramachandran diagram. Ser-293 is the only outlier in both structures.

Overall structure

There are four full-length protein molecules in the unit cell of both the binary and tertiary IRAK complexes in the triclinic *P*1 space group. These protein molecules take essentially the same conformation and are superimposable with an r.m.s.d. of <0.20 Å over 420 Cα atoms. Their structures are very well defined by continuous electron densities from the N to C terminus with few rotameric or torsional errors, except for Ser-293 that remains as a Ramachandran outlier as observed in all the previous *bs*MenE structures (PDB code 3ipl) (23, 24). In each unit cell, two homodimers (chains A and C form one dimer and chains B and D form another dimer) are formed by back-to-back contacts of the N-domains (residues 1–379) of the monomers, whereas an active site is formed far from the dimer interface between the N- and C-domains (residues 393–486) with participation of the residues from the linker (residues 380–392) and binds an OSB-NCoA ligand in each monomer (Fig. 2).

Interestingly, the two OSB-NCoA ligands in any homodimer exhibit significant differences in the ribose ring together with the associated 3′-phosphate, whereas their acyl group and the amino pantetheinyl group are superimposable with exactly the same orientations (Fig. 2, *D*–*F*). Take one dimer of either complex as an example: the ribose ring of OSB-NCoA takes a normal *endo*-pucker conformation with the C3′-phosphate at the axial position in chain C (Fig. 2*E*), and the 3′-phosphate of chain A in the same dimer occupies the equatorial position in an almost flat ribose ring (Fig. 2*D*). This difference is caused by

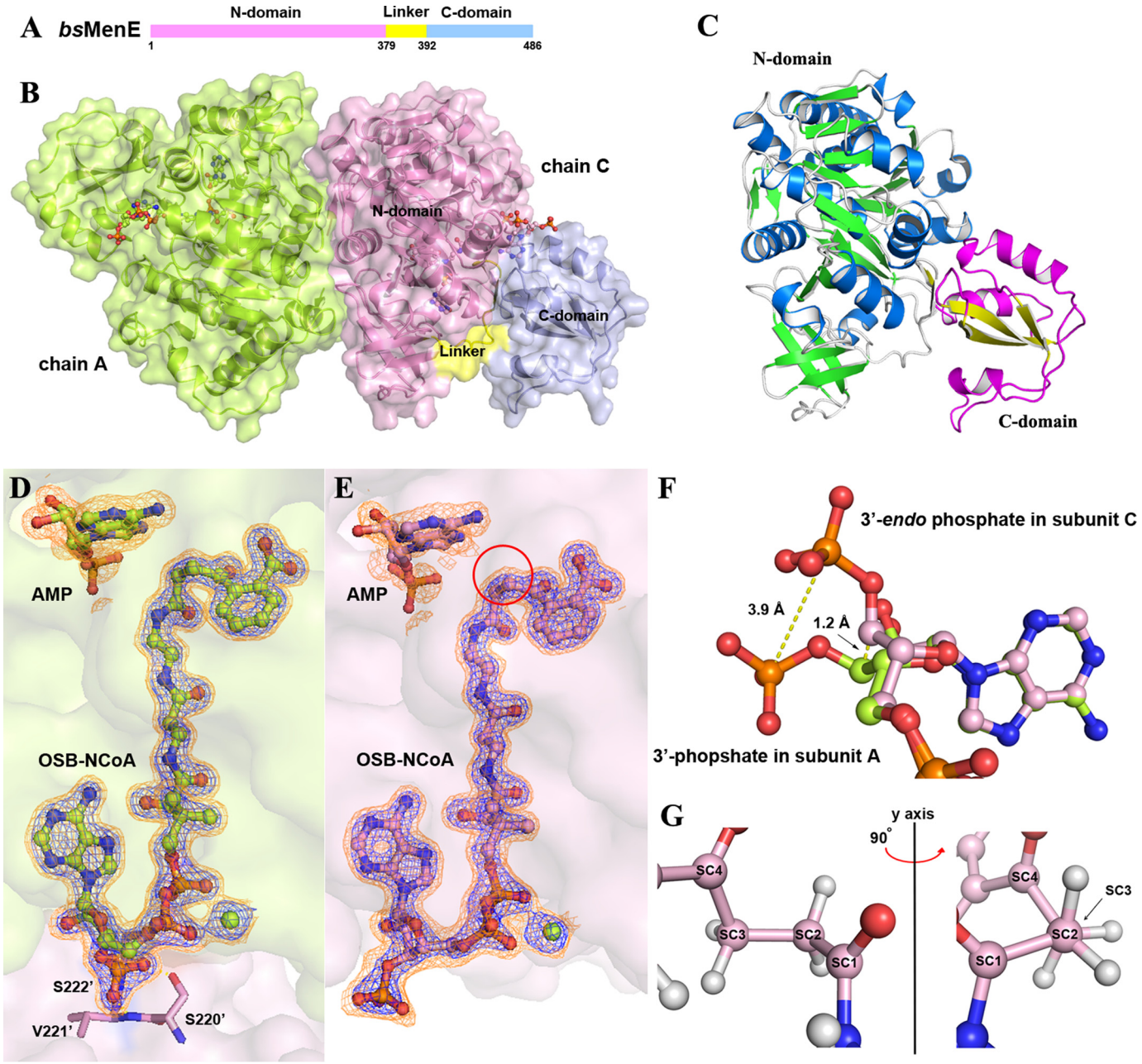

Figure 2. Overall structure of the *bs*MenE–OSB-NCoA–AMP ternary complex. *A*, two-domain organization of *bs*MenE. *B*, surface and schematic representation of the functional dimer. Chain C is colored according to the domains shown in *A*, and the ligands OSB-NCoA and AMP are represented in *ball-and-stick* mode. *C*, tertiary folding of a *bs*MenE subunit in the ternary structure. The structure is presented in the same orientation as chain C in *B* with *blue* α-helices and *green* β-sheets in the N-domain and with *magenta* α-helices and *yellow* β-sheets in the C-domain. *D*, OSB-NCoA and AMP in chain A. The CoA 3′-phosphate interacts with three residues (Ser-220′, Val-221′, and Ser-222′) from the neighboring unit cell. *E*, OSB-NCoA and AMP in chain C. *D* and *E*, ligands are represented in *ball-and-stick* with $2mF_o - DF_c$ density map contoured at 2.0 σ (*blue mesh*) and 1.0 σ (*orange mesh*). *F*, superimposed OSB-NCoA ligands from chain C and chain A. The different orientation of the 3′-phosphate is highlighted. *G*, two views of the *gauche* ethylene group in the succinyl moiety of OSB-NCoA. The presented structure is highlighted in a *red circle* in *E*.

three hydrogen bonds between the chain A 3′-phosphate with the backbone or side chain of Ser-220′, Val-221′, and Ser-222′ from chain C′ of the neighboring unit cell (Fig. 2*D*), whereas such crystal packing interactions are not found for the chain C ligand (Fig. 2*E*).

Moreover, the two dimers in the unit cell of the ternary complex are different, of which the dimer including chain A and chain C contains AMP in each chain (Fig. 2, *D* and *E*) and the other dimer contains no AMP similar to those in the binary complex. AMP in the former dimer has a low occupancy (0.60 in chain A and 0.58 in chain C) and is much poorer in electron density compared with OSB-NCoA. For simplicity, chain D of the binary complex and chain C of the ternary complex without the crystal packing interactions are used as the representatives of the two complexes.

Thioester-forming conformation

Although both IRAK complexes maintain the same topology and di-domain folding as the previously determined *bs*MenE structures (24, 26), their C-domains are oriented very differ-

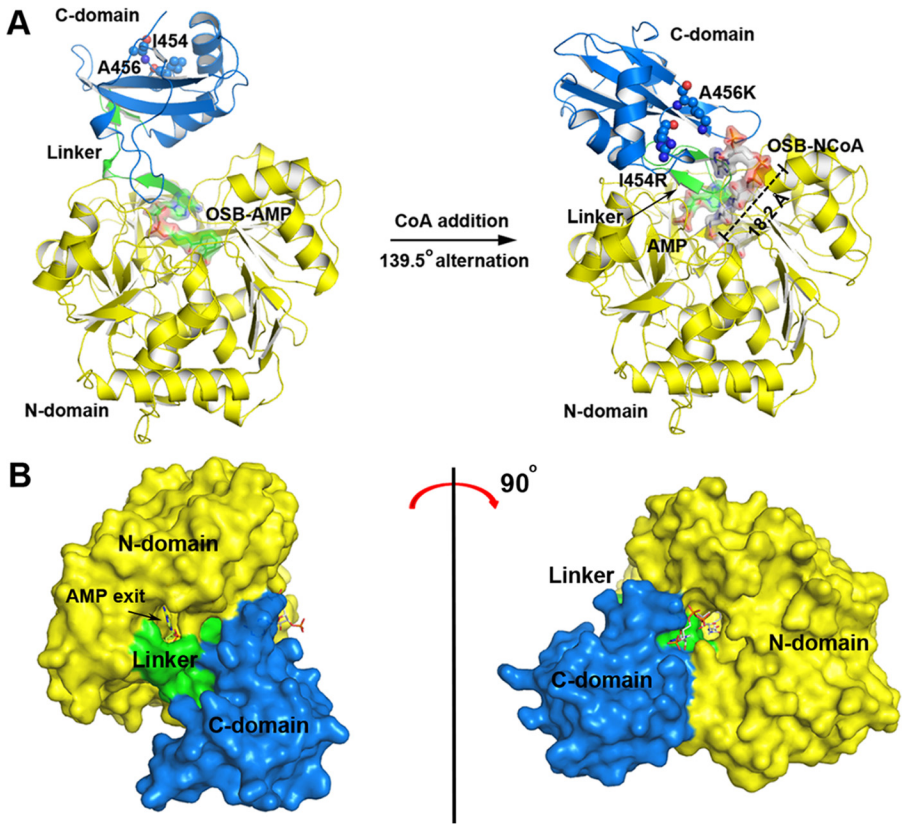

Figure 3. Comparison of the *bs*MenE-OSB-NCoA-AMP structure in a thioesterification conformation with the *bs*MenE-OSB-AMP structure in an adenylation conformation. *A,* 139.5° difference in orientation of the C-domain (*blue*) between the two structures. The large N-domains (*yellow*) are superimposable and drawn in exactly the same way in the two structures, and the inter-domain linker (379–392) is colored in *green*. The two mutated residues I454R and A456K are denoted as *spheres*. The U-shaped OSB-AMP (*green surface*) represents the adenylate tunnel in adenylation conformation (*left*) and is fragmented into AMP (*green surface*) and OSB-CoA (represented by OSB-NCoA, *white surface*) in the thioesterification conformation (*right*). *B,* two views of the *bs*MenE-OSB-NCoA-AMP ternary structure in surface representation. The *left view* shows one end of the interconnected ligand-binding tunnel where AMP (*sticks*) is bound, and the *right view* shows the other end of the tunnel where the ADP moiety of the OSB-NCoA (*sticks*) is exposed to the bulk solution. The protein surface is colored according to domains as shown in *A*.

ently relative to the large N-domains. These new structures are, however, closely similar to that of 4CBL (9), ACS (8), and ACSM2A (19) in a thioesterification state. This comparison clearly shows that the IRAK complexes take a thioesterification conformation dedicated for the second half-reaction. In these IRAK complexes, a compact domain interface with a 1021.8 Å^2 surface is formed from many N-domain residues and residues on one side of the C-domain. In comparison, a smaller interdomain interface (~751.5 Å^2) is formed between the same set of N-domain residues and residues on the other side of the C-domain of *bs*MenE in the pre- and post-adenylation states (23, 26). As calculated by the DynDom server (29), the C-domain rotates by 139.5° from its position in the adenylation conformation to that in the ligand-bound IRAK structures, hinging on Ser-384 in the linker region (Fig. 3*A*). To accommodate this C-domain rotation, the Ser-384 dihedral angles Φ and Ψ drastically change from −62.4 to −110.5° and from −9.3 to −24.4°, respectively.

The large C-domain rotation significantly reconfigures the enzyme active site, which binds the AMP product and OSB-NCoA product analogue in two interconnected, perpendicular tunnels (Fig. 3*A*). One tunnel binds the AMP and the benzoic acid moiety of the OSB-NCoA ligand in the same positions as the corresponding components of OSB-AMP in the adenylation conformation (26) and is thus referred to as the adenylate tunnel. The other tunnel is linear and binds the amino pantetheinyl portion of the OSB-NCoA analogue, which is thus referred to as the CoA tunnel. The adenylate and CoA tunnels meet at the mid-point of the former, where the succinyl group is twisted at a nearly vertical angle with its SC2–SC3 ethylene group taking an energetically unfavorable *gauche* conformation and links the amino-CoA moiety to the benzoic acid moiety in the OSB–NCoA ligand (Fig. 2*G*). The product analogue is thus bound as a crowbar and is unable to dissociate from the protein if the interdomain interface is not disassembled (Fig. 3*A*).

The adenylate tunnel contains AMP close to the protein surface and exposes it to the solvent, whereas the CoA tunnel is also open to solvent at one end and exposes the 3′-phosphoryl-ribosyl group of the adenosine diphosphate moiety of the OSB-NCoA product analogue in the bulk solution (Fig. 3*B*). As noted earlier, OSB-NCoA is unable to dissociate from the protein in the thioesterification conformation due to its unique binding mode, whereas AMP is easy to escape to the bulk solvent due to the absence of blocking barriers in the exit channel. From this difference, it is obvious that AMP is released from the enzyme active site ahead of OSB-CoA after the two products are formed from the thioesterification reaction. This is consistent with the absence of the AMP product in one dimer and the considerably

poorer electron density for AMP relative to OSB-NCoA in the other dimer in the unit cell of the ternary IRAK complex (Fig. 2, *D* and *E*).

Adenylate tunnel

In the adenylate tunnel (Fig. 3*A*), AMP in the ternary IRAK structure forms the same interactions with the N-domain as the AMP moiety of the OSB-AMP intermediate in the *bs*MenE-OSB-AMP structure; its adenine ring is sandwiched between the phenolic side chain of Tyr-286 and the backbone of Gly-263–Gly-264–Gly-265, although its 6-amino group forms a hydrogen bond with the backbone carbonyl group of Ser-285, and its 2′- and 3′-hydroxyl groups form hydrogen bonds with the Asp-367 side-chain carboxylate. However, AMP has no interactions with the C-domain or the linker region. In contrast, the AMP moiety of OSB-AMP forms hydrogen bonds with Arg-382 of the linker region and Lys-471 of the C-domain in the *bs*MenE-OSB-AMP structure (26). Thus, AMP is significantly weakened in its interaction with the enzyme in the thioesterification conformation after remodeling of the adenylate tunnel, thus facilitating its release from the thioesterification active site. Another important change in the remodeled adenylate tunnel is the drastic rearrangement of the His-196 side chain, which forms a hydrogen bond with the bridging oxygen atom of OSB-AMP intermediate in the *bs*MenE-OSB-AMP structure but is reoriented by 37° to form an inter-domain hydrogen bond with Glu-392 of the C-domain in the thioesterification conformation. This movement of His-196 connects the adenylate tunnel and CoA tunnel together and exposes the OSB-AMP intermediate to the attack of the CoA substrate. This gate-keeping function of His-196 is consistent with that of the equivalent residues in other ANL enzymes (9, 20).

The OSB-binding pocket is little changed in the adenylate tunnel remodeling by the large C-domain rotation because it is formed entirely by N-domain residues and is buried deep inside the protein. As shown in Fig. 4, it is composed of amino acid residues specifically conserved among MenE orthologues and forms the same binding interactions for the benzoic acid moiety of OSB-NCoA as those found in the *bs*MenE-OSB-AMP structure (26). Nonetheless, the newly solved IRAK–OSB–NCoA complex structure at 1.76 Å resolution reveals that water molecules are involved in the binding interaction. Specifically, the aromatic carboxylate of the ligand is stabilized through hydrogen bonding with three well-defined water molecules O1, O2, and O3 (Fig. 4*A*), of which O1 forms an additional hydrogen bond with the Ser-237 side chain and O2 further hydrogen-bonds with the side chains of Ser-293 and Gln-294. These water-mediated interactions were not identified in the previously solved structure at a lower resolution (26).

CoA-binding tunnel

The large C-domain rotation in reconfiguration of the enzyme active site creates a new tunnel at the domain interface for binding of the amino-CoA moiety of the OSB-NCoA ligand. Its major portion is linear and extends 18.2 Å from the protein surface to the adenylate tunnel at a vertical angle (Fig. 3*A*), whereas its minor part is non-continuous to the linear portion and allows the amino CoA moiety of OSB-NCoA to bind in a hairpin conformation. The adenine ring at one end of the ligand hairpin is inserted between the aromatic side chains of Tyr-452 and Trp-422 to form a strong π–π stacking interaction. This adenine ring is further stabilized by polar interactions, including hydrogen bonds with the side chain hydroxyl of Ser-389, ϵ-NH_2 of Lys-86, and the carbonyl oxygen in the pantoic moiety at 6′-NH_2 (Fig. 4*A*).

The 3′-phospho-ADP moiety of the ligand, which forms the "U" turn and links the pantetheinyl group to the adenine ring, is exposed in the solvent (Fig. 3*B*). The diphosphate group in the ADP moiety forms hydrogen bonds with four water molecules (O5, O9, O10, and O12) and chelates a Mg^{2+} ion, which is further coordinated with the backbone carboxyl group of Phe-219 and three additional water molecules (O6, O7, and O8) to form a clearly defined octahedral coordination sphere (Fig. 4*A*). These interactions with water and the metal ion help to position the diphosphate in a conformation to make ~90° turn in the formation of the hairpin structure. Similar Mg^{2+} chelation to the diphosphate group of the CoA ester ligand is found in 4CBL, which, however, only interacts with the α-phosphate of the CoA moiety and forms a square-planar coordination system with three additional water molecules (9). In contrast, no metal is chelated to the diphosphate group of the CoA ligand in all other known crystal structures of acyl/aryl-CoA synthetases in the thioesterification conformation.

The 18.2 Å linear binding tunnel of the pantetheinyl group is composed of residues from both N- and C-domains and binds the ligand with extensive van der Waals interactions and a few polar interactions. As shown in Fig. 4*A*, a tripeptide fragment, Leu-192–Pro-193–Leu-194, and a β-hairpin motif consisting of residues 237–243 from the N-domain form extensive van der Waals contacts with the ligand. In addition, a β-hairpin loop (Ser-389–Gly-390–Gly-391–Glu-392 from the linker region, designated as the SGGE motif) forms multivalent interactions with the ligand. Specifically, the backbone carbonyl oxygen atoms of Gly-390 and Gly-391 form hydrogen bonds with the nitrogen atoms of the two pantetheine amide groups, whereas the side chain ethylene group of Glu-392 forms van der Waals contacts with the β-alaninyl moiety of the pantetheinyl group. Besides these direct binding interactions, two water molecules, O4 and O13, are also involved in the ligand binding via hydrogen bonds (Fig. 4*A*).

Mutation of active-site residues

We mutated the conserved amino acid residues *underlined* in Fig. 4*A* to understand their contribution to the formation of the thioesterification conformation and the enzymatic catalysis. The resulting site-directed mutants, including S198A, S384P, S389A, E392A, W422A, and Y452A, were readily expressed and purified to homogeneity like the wild-type *bs*MenE. The pure mutant proteins were found similar to the wild-type enzyme in circular dichroism spectrometry without significant changes of the secondary structure.

The single-substrate steady-state kinetic constants (k_{cat} and K_m) were determined by varying the concentration of one substrate while keeping the other two substrates at a saturated concentration for the wild-type *bs*MenE and its mutant proteins (Table 1). Interestingly, no detectable activity was found

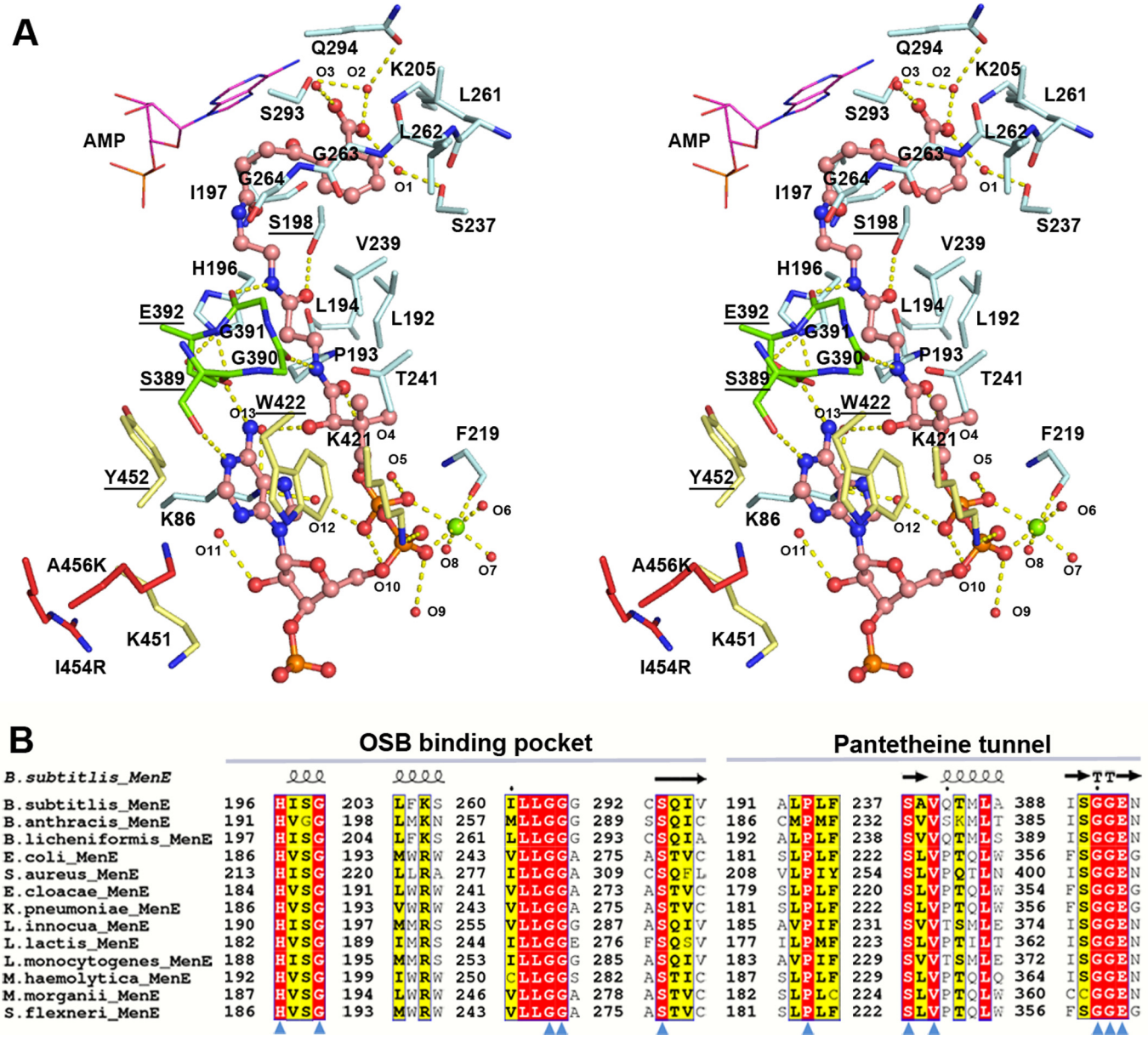

Figure 4. Active site of the *bs*MenE thioesterification conformation. *A,* stereo diagram of the OSB-CoA-binding pocket. The ligand OSB-NCoA is represented as *balls and sticks* with its carbon atoms colored in *pink*. The nucleotide AMP is shown as *magenta lines*. The carbon atoms of the active-site residues from N-domain (1–379), linker (380–392), and C-domain (393–486) are respectively colored *pale-cyan, green,* and *pale-yellow,* except the two mutated residues I454R and A456K are highlighted in *red*. The water molecules that directly interact with OSB-NCoA or active-site residues are shown as *red dots,* and the magnesium ion is shown as a *green sphere*. The *yellow dashed lines* denote hydrogen bonds with a distance shorter than 3.5 Å. The oxygen, nitrogen, and phosphorus atoms in the whole panel are colored *red*, *blue,* and *orange*, respectively. The water molecules O1–O13 correspond to HOH14, HOH35, HOH1472, HOH791, HOH412, HOH238, HOH1513, HOH1482, HOH1055, HOH1821, HOH101, HOH875, and HOH239 of the ternary structure (chain C), respectively. The *underlined* residues have been mutated for kinetic studies. *B,* alignment of sequence fragments contributing to binding of the OSB moiety and the pantetheinyl group of OSB-NCoA. Secondary structural elements are shown for the *bs*MenE complex containing OSB-NCoA and AMP in the alignment. Residues conserved in 100, 100 to 95, and 95 to 80% sequences are represented with *blue triangles*, marked with *red boxes*, and shown in *yellow background*, respectively.

for the mutants S384P, W422A, and Y452A, demonstrating the absolute requirement of these residues for the enzymatic catalysis. S384P loses the activity likely due to the fact that a proline residue is unable to serve as a hinge residue, whereas W422A and Y452A lose their activity likely due to elimination of the π-π stacking interaction between the aromatic residues and the adenine ring of the CoA ligand (Fig. 4*A*). In contrast, the S198A and S389A mutations cause no more than 14-fold decrease in catalytic efficiency (k_{cat}/K_m) for all substrates, although both Ser-198 and Ser-389 form a hydrogen bond with the pantetheinyl group of OSB-NCoA (Fig. 4*A*). However, the alanine substitution of Glu-392, which has no direct interaction with the bound CoA ligand but forms a hydrogen bond with His-196 to open the adenylate tunnel for access of the CoA substrate to the OSB-AMP intermediate, reduces the catalytic efficiency by 3 orders of magnitude for CoA–SH and 2 orders of magnitude for OSB and ATP. This significant activity loss sharply contrasts the results for the H196F mutant, which also eliminates the Glu-392–His-196 interaction but essentially retains all the activity of the wild-type enzyme (26). One possible expla-

Table 3
Adenylation rates of *bs*MenE and its mutants

Protein	Adenylation rate	Relative activity
	$\mu M \cdot min^{-1}$	%
Wild type	86 ± 5	100 ± 5
S198A	50 ± 1	59 ± 1
S384P	11 ± 3	13 ± 4
S389A	64 ± 4	74 ± 4
W422A	65 ± 4	76 ± 5
Y452A	59 ± 1	69 ± 1
I454R	76 ± 4	88 ± 4
I454R/A456K	64 ± 1	74 ± 2

nation for this difference is that the unconstrained His-196 side chain in the E392A mutant may interact with the pantetheinyl group or residues in the CoA tunnel to affect CoA binding and thus significantly reduces the catalytic activity, whereas the unconstrained Glu-392 or Phe-196 side chain in the H196F mutant has no such adverse effects and causes much less activity loss. In this possible scenario, Glu-392 plays the role of restricting the His-196 side chain from forming adverse interactions with the substrate or other active-site residues.

We also determined the reaction rate of the first adenylation half-reaction for the site-directed mutants and the crystallization-enhancing mutants in comparison with the wild-type enzyme. As shown in Table 3, except that S384P possesses 13% of the adenylation activity of the wild-type enzyme, all other mutants are comparable with the wild-type enzyme (≥59%) in adenylation rate. Because S384P loses the activity to form the final product OSB-CoA in the steady-state experiment (Table 1), its retention of 13% adenylation activity shows the importance of the Ser-384 backbone flexibility to the domain movement in forming the thioesterification and adenylation conformations, of which the former is affected much more than the latter. For all other mutants, the comparable adenylation rates clearly show that activity decrease in the steady-state kinetic experiments (Table 1) is mainly due to the mutational effects on the second half-reaction, thioesterification, via the loss of the binding interactions specific in the thioesterification conformation (Fig. 4*A*). Because these mutated residues are not involved in forming the adenylation-active site (23, 24, 26), the kinetic data unambiguously demonstrate the thioesterification-specific effects of the mutated residues and provide strong support for re-configuration of the active site for thioesterification half-reaction through domain alternation. Most clear-cut results were obtained for the W422A and Y452A mutant proteins, of which the adenylation reaction rates are essentially unaffected and yet the activities to form the thioesterification products are completely eliminated. Although similar thioesterification-specific mutational effects have been provided previously for thioesterification active-site residues in homologous enzymes with steady-state kinetics (10, 11), the current mutational results provide the most direct evidence.

Discussion

As a member of the ANL enzyme family, OSB-CoA synthetase (MenE) is a valuable drug target in the vitamin K biosynthetic pathway. In this study, we have determined high-resolution crystal structures of a catalytically competent double mutant (IRAK) of *bs*MenE in complex with a stable product analogue, OSB-NCoA, and a combination of OSB-NCoA and AMP. They are found to take a thioester-forming conformation, which results from a 139.5° rotation of the small C-domain around the hinging residue Ser-384 from its position in the previously determined *bs*MenE adenylation conformation (24, 26). Interestingly, the product analogue takes a crowbar-like shape and tightly binds to the protein in an energetically unfavorable conformation, whereas AMP loosely binds to the protein with easy access to the bulk solvent. These features of the ligand binding strongly support a sequential product release in which AMP is released before OSB-CoA, in contrast to the results from previous kinetic studies that suggest that OSB-CoA is released before AMP (22). In addition, these crystal structures revealed the amino acid residues contributing to recognition and binding of the substrates and products in the thioesterification reaction. Site-directed mutagenesis showed that these residues significantly affect the thioesterification half-reaction but have negligible effects on the adenylation half-reaction. These results have not only provided unambiguous support for the domain-alternation catalytic mechanism of ANL enzymes in general, they have also revealed the unique thioesterification active site of OSB-CoA synthetases and provided the structural basis for their catalysis of the thioesterification reaction to facilitate their utility as a drug target.

The *bs*MenE thioester-forming structure is very similar to those of other ANL family members in folding and C-domain orientation. Its closest structural orthologue is *Nicotiana tabacum* 4-coumarate-CoA ligase (4-CCL) (20) with r.m.s.d. of 1.66 Å and a sequence identity of 30.08%. Despite this structural similarity, these homologous enzymes contain only a limited set of conserved amino acid residues such as His-196 and Glu-392 that form a hydrogen-bonding pair in *bs*MenE (Fig. 4*A*). In contrast, most active-site residues are conserved specifically among the MenE family, including those responsible for binding the OSB moiety of OSB-NCoA in the previously identified the OSB-binding site (24). The residues responsible for binding the pantetheinyl group of OSB-NCoA in *bs*MenE are also found to be specifically conserved among 200 unique MenE sequences with sequence identity from 25 to 50% identified by BLAST from the UniProtKB database (30) using *bs*MenE as query and setting the E-threshold at 0.01 (Fig. 4*B*).

Interestingly, the IRAK complex structures reveal a distinct binding mode for CoA and its derivatives, which recognizes CoA as a hairpin with its polar 3′-phospho-ADP head inserted firmly into the C-domain of the thioesterification conformation (Fig. 5*A*). This CoA-binding mode is similar to that observed in 4CBL (9) but different from all other known ANL enzymes with a CoA or CoA ester in the thioesterification conformation, including human ACSM2A (19), *Salmonella enterica* acetyl-CoA synthetase (ACS) (8), and 4-CCL (20), in which the polar head of the CoA hairpin is turned by ~180° and bound to the N-domain (Fig. 5, *B–D*). This different CoA-binding mode is due to the structural difference in the 3′-phospho-ADP-binding motifs of the enzymes. In *bs*MenE (Fig. 5*A*) and 4CBL (9), the polar CoA headgroup is bound by the $\pi-\pi$ interaction with two conserved aromatic residues and the electrostatic interaction with a positively charged groove on the C-domain surface (Fig. 5*A*). In comparison, other acyl/aryl-CoA synthetases con-

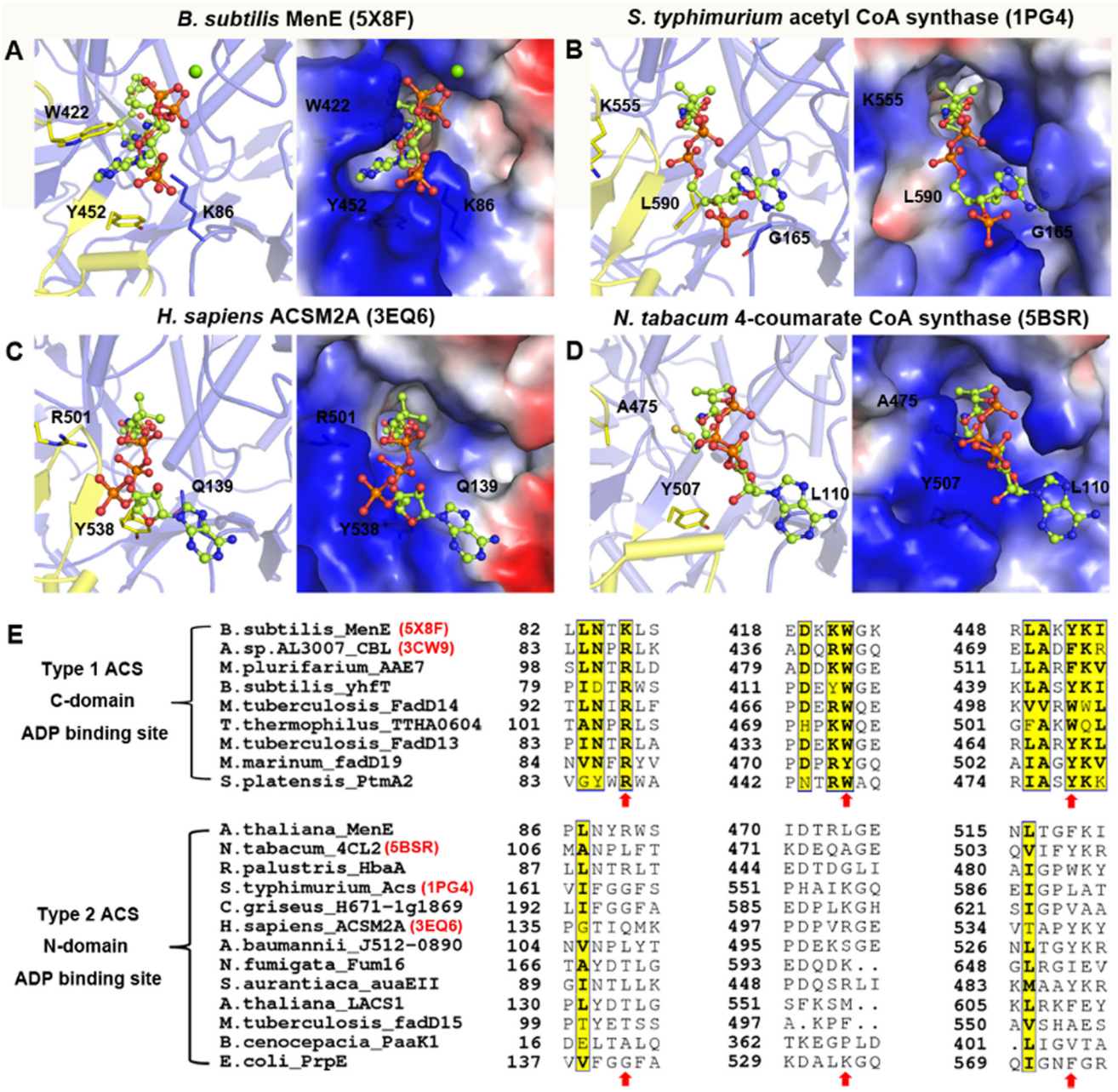

Figure 5. Two CoA-binding modes in different ACS. *A,* 3′-phospho-ADP moiety of CoA binding to the C-domain in *bs*MenE (PDB code 5X8F). *B,* 3′-phospho-ADP moiety of CoA binding to the N-domain in *S. enterica* acetyl-CoA synthetase (PDB code 1PG4). *C,* 3′-phospho-ADP moiety of CoA binding to the N-domain in human medium chain acyl-CoA synthetase (ACSM2A, PDB code 3EQ6). *D,* 3′-phospho-ADP moiety of CoA binding to the N-domain in *N. tabacum* 4-coumarate-CoA ligase (PDB code 5BSR). The shown structures are from the same areas of the crystal structures of the ligand-bound proteins that have been aligned according to their N-domains. *A–D*, proteins are represented in schematic with a *light-blue* N-domain and a *pale-yellow* C-domain (*left*) and in electrostatic potential surface (*right*), and the CoA ligand is shown in *balls-and-sticks,* and the Mg^{2+} ion is presented as a *green sphere*. *E,* sequence alignment of the peptide fragments involved in binding of the 3′-phospho-ADP moiety. Structurally determined members with a CoA derivative are labeled with the corresponding PDB codes shown in *parentheses* (*red*). The *red arrows* point to the three conserved residues or their equivalents in the sequence alignment, which are shown or labeled in *A–D*.

taining a CoA or CoA ester have no similar structural features on the C-domain. Instead, they contain an extensive positive electrostatic potential groove in the N-domain for the binding of the CoA headgroup, which is also present but blocked for CoA binding by a bulky residue in *bs*MenE (Lys-86, Fig. 5*A*) and 4CBL (Arg-87). The metal binding found in *bs*MenE (Fig. 5*A*) and 4CBL, which is absent in other known structures of acyl/aryl-CoA synthetases containing a CoA or CoA derivative (Fig. 5, *B–D*), changes the surface charge on the ADP group of CoA and may also prevent it from binding to the N-domain.

According to the mode of CoA binding and the associated binding motifs, two subtypes of acyl/aryl-CoA synthetases are found in 22 representatives selected from acyl-CoA synthetases in the CATH6 superfamily 3.30.300.30 (31) and structurally solved acyl/aryl-CoA synthetases after excluding redundant sequences and sequences unreviewed in the UniProtKB database. The type I synthetases bind CoA with its polar headgroup

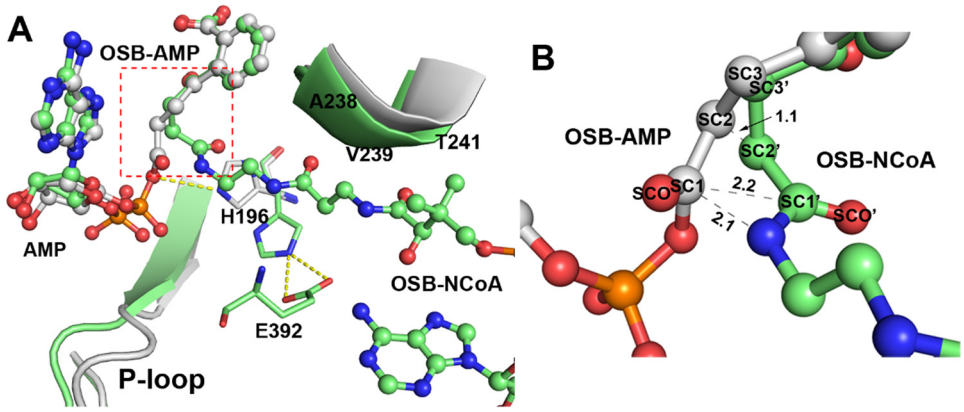

Figure 6. Modeling of the OSB-AMP intermediate into the thioesterification conformation. *A,* superimposed *bs*MenE-OSB-AMP and the IRAK–OSB-NCoA–AMP structure. The structures are colored in *gray* for the former (chain A, PDB code 5GTD) and *pale-green* for the latter (chain C, PDB code 5X8F). Ligands OSB-AMP, OSB-NCoA, and AMP are represented as *balls-and-sticks*. P-loop and the helical segment (Ala-238–Val-239–Gln-240–Thr-241) are different in the two structures and are shown in the schematic. The His-196 side chain takes a different orientation in the two structures, and both conformations are shown in *sticks*, and its hydrogen bonds with Glu-392 (in *sticks*) are denoted by *yellow dashed lines*. *B,* amplified view of OSB-NCoA and the modeled OSB-AMP. The area shown corresponds to the rectangular region *circled* by *red dashes* (*A*) with a slightly adjusted perspective.

inserted into the C-domain as found for *bs*MenE and 4CBL and are characterized by the two conserved aromatic residues and an N-domain-blocking bulky residue corresponding to Trp-422, Tyr-452, and Lys-86 in *bs*MenE, respectively (Fig. 5*E*). This group of enzymes is also characterized by Mg^{2+} binding to the ADP group and by the residues contributing to the positive electrostatic potential groove on the C-domain (Fig. 5*A*). They include the majority of MenE orthologues and other acyl/aryl-CoA synthetases such as YhfT from *B. subtilis* (UniProtKB O07619) or FadD13 from *Mycobacterium tuberculosis* (32). In contrast, the type II synthetases bind CoA with its polar head-group bound to the N-domain and without metal chelation and are characterized by the absence of the conserved sequence motifs for the type I synthetases (Fig. 5*E*). Besides the three enzymes structurally determined for their thioesterification conformations in complex with a CoA or its derivative (8, 19, 20), the type II enzymes include a few MenE orthologues such as MenE from *Arabidopsis thaliana* (33) and other acyl/aryl-CoA synthetases such as PaaK1 from *Burkholderia cenocepacia* (34). Noticeably, all MenE orthologues from pathogenic bacteria are type I enzymes, and their distinct CoA-binding mode as found in *bs*MenE may be explored for development of new antibiotics in the future.

Besides shedding light on the unique CoA recognition mode, the IRAK complex structures also offer the template for modeling of OSB-AMP, the other substrate of the thioesterification half-reaction, into the thioesterification active site. This modeling is achieved manually by superimposing the OSB-AMP-bound N-domain of the post-adenylation *bs*MenE structure to the N-domain of the IRAK complex structure and leave the OSB-AMP ligand in the IRAK structure after removing the post-adenylation protein structure. As shown in Fig. 6, the AMP product and the benzoic acid moiety of the OSB-NCoA overlap very well with the corresponding structural components of the modeled OSB-AMP intermediate. Interestingly, the succinyl carbonyl carbon atom (SC1) of the OSB-AMP intermediate is located 2.1 Å from the nitrogen atom of OSB-NCoA, which corresponds to the nucleophilic thiol group of free CoA–SH when it is bound to the CoA-binding tunnel like the CoA moiety of the product analogue. This close distance should allow OSB-AMP and CoA–SH to react readily to form the S–C thioester bond (~1.82 Å) in the OSB-CoA product. Thus, this modeled structure offers an opportunity to speculate on how the two substrates are arranged and positioned for the thioesterification reaction in the domain-alternated conformation.

The succinyl group is basically extended and linear in the modeled OSB-AMP (26), whereas it is twisted in a *gauche* conformation in the OSB-NCoA product analogue (Fig. 2*G*). This strained ligand structure is unlikely due to the mutations in the protein because both mutated residues are far away from the active site and make no contact with the ligand (Fig. 4*A*). This difference in the ligands indicates that the reacting groups, particularly the carbonyl group (SC1-SCO) in the adenylate intermediate, must undergo a long-distance movement of ~4.0 Å as suggested by the positional difference of the oxygen atom before and after the thioesterification reaction (Fig. 6). It is not clear at present how this large movement is accommodated in the thioesterification process. Noticeably, there is no suitable polar group nearby to interact with the carbonyl oxygen and activate the acyl group in the modeled OSB-AMP for the thiolation reaction with CoA–SH. This activating group may be hidden due to deviation of the modeled structure from the genuine structure. Alternatively, its absence may be due to the fact that OSB-AMP is active enough for the thiolation reaction and needs no further activation.

After the thioesterification reaction, the AMP product is released first, but OSB-CoA or its analogue cannot be released before disassembly of the thioesterification conformation, due to the different binding modes noted earlier for the products (Figs. 2, *D* and *E*, and 4*A*). This difficulty in product release is fully consistent with the finding that product release is the rate-limiting step in the MenE-catalyzed reaction in a previous kinetic study (22). In this connection, it should be noted that the succinyl group is strained in a *gauche* conformation in the OSB-NCoA product analogue. The release of this strained conformation is thus proposed to assist or even drive the disassembly of the interdomain interface and eventually the whole thioes-

Table 4
Synthetic primers for cloning and site-specific mutation of *bs*MenE

Protein	Oligonucleotide sequence (the mutated codons are underlined)
WT	
Forward	CATGCCATGGGCATGCTGACAGAACAGCCCAACTGG
Reverse	CCGCTCGAGTCATAGCAGTTCTCCTTTACGCGC
S198A	
Forward	GCCGCTCTTTCATATCGCCGGATTGTCCGCATTAT
Reverse	ATAATGCGGACAATCCGGCGATATGAAAGAGCGGC
S384P	
Forward	ATATGTATTAGACAGACGTCCAGATCTGATCATATCCGGCGG
Reverse	CCGCCGGATATGATCAGATCTGGACGTCTGTCTAATACATAT
S389A	
Forward	CGTTCAGATCTGATCATAGCCGGCGGAGAAAACATTTA
Reverse	TAAATGTTTTCTCCGCCGGCTATGATCAGATCTGAACG
E392A	
Forward	CTGATCATATCCGGCGGAGCAAACATTTATCCGGCCG
Reverse	CGGCCGGATAAATGTTTGCTCCGCCGGATATGATCAG
W422A	
Forward	GGCTGAGGACAAAAAAGCGGGGAAAGTGCCTCACG
Reverse	CGTGAGGCACTTTCCCCGCTTTTTTGTCCTCAGCC
Y452A	
Forward	AGAACGCTTGGCGAAG GCT AAAATTCCGGCAAAAT
Reverse	ATTTTGCCGGAATTTT AGC CTTCGCCAAGCGTTCT
I454R	
Forward	GAACGCTTGGCGAAGTATAAAAGACCGGCAAAATTCTTTGTGCTTGACCG
Reverse	CGGTCAAGCACAAAGAATTTTGCCGGTCTTTTATACTTCGCCAAGCGTTC
I454R-R456K	
Forward	GAACGCTTGGCGAAGTATAAAAGACCGAAAAAATTCTTTGTGCTTGACCG
Reverse	CGGTCAAGCACAAAGAATTTTTTCGGTCTTTTATACTTCGCCAAGCGTTC

terification conformation for the enzyme to release the OSB-CoA product and return to a ligand-free state to complete a catalytic cycle.

In summary, we have for the first time determined the crystal structure of a catalytically competent MenE mutant in complex with the OSB-NCoA product analogue or both AMP and OSB-NCoA in the thioesterification conformation. These crystal structures define a 139.5° C-domain rotation in configuration of the thioesterification conformation from the adenylation conformation containing the adenylate intermediate OSB-AMP, and they provide strong support for the domain-alternation mechanism of the ANL enzymes. They have revealed a distinct mode for interaction with the CoA substrate in comparison with other acyl/aryl-CoA synthetases and have enabled identification of active-site residues discretely conserved among MenE orthologues. In addition, these structures have also revealed that the product is dead-locked in the thioesterification conformation with a strained conformation, raising the possibility that release of the strained energy in the product ligand may be a pre-installed molecular mechanism to release the product and disassemble the thioesterification conformation to complete a catalytic cycle. Moreover, the product analogue-bound structures allow modeling of the adenylate intermediate OSB-AMP in the thioesterification conformation to illuminate how the second half-reaction occurs in members of the MenE enzyme family. These results have provided fresh insights into the domain-alternation mechanism of the essential vitamin K biosynthetic enzyme and its homologues in the ANL enzyme family.

Experimental procedures

Expression and purification of bsMenE and its mutants

The *bs*MenE used in this study contained only the wild-type sequence, which is different from the protein used in previous studies with a hexahistidine tag at either the N or C terminus (23, 24, 26). The *menE* gene was amplified from the genomic DNA of *B. subtilis* strain 168 using primers listed in Table 4 and cloned into the pET28a expression vector using the restriction sites of NcoI and XhoI. After the gene sequence was confirmed by DNA sequencing (Beijing Genomics Institute, Shenzhen, China), the plasmid construct was transformed into *Escherichia coli* strain BL21 (DE3). For protein expression, cells were grown in 2 liters of Luria-Bertani broth (LB) at 37 °C to reach an A_{600} of 0.8 before induction with 0.2 mM isopropyl β-D-thiogalactoside for protein overexpression at 18 °C for 20 h. For purification, the harvested cells were homogenized by sonication in 25 mM Tris buffer (pH 8.0). After high-speed centrifugation at 18,000 rpm for 50 min, the supernatant was fractionated by ammonium sulfate, and proteins precipitated by the salt at a concentration from 50 to 60% saturation were collected. Following desalting, *bs*MenE was purified from the precipitated protein fraction on a HiPrep DEAE FF 16/10 column (GE Healthcare) using a slow salt gradient from 0.11 to 0.20 M NaCl in 25 mM Tris buffer (pH 8.0) at a flow rate of 2 ml/min over 90 min. The collected *bs*MenE fractions were combined, concentrated, and further purified by size-exclusion chromatography. The obtained protein was greater than 95% pure as assessed by SDS-PAGE and was concentrated and stored until use at −80 °C in the buffer containing 25 mM Tris, 200 mM NaCl, and 10% glycerol (pH 8.0). The protein concentration was measured using Pierce™ Coomassie protein assay kit. All the buffers used in the purification process contained 2.0 mM 2-mercaptoethanol.

Point mutations were introduced into *bs*MenE to obtain mutant proteins S198A, R382P, S384P, S389A, E392A, W422A, Y452A, I454R, and I454R/A456K using the *bs*MenE-expressing plasmid in the pET28a vector as template and primers listed in

Table 4 for mutagenic reactions using the QuikChange™ mutagenesis kit (Stratagene). The genes of the mutant proteins were fully sequenced by Beijing Genomics Institute to confirm that only the desired point mutations were introduced. These mutant proteins were expressed and purified with the procedures described above for the wild-type protein and were all shown to present a secondary structure similar to that of the wild-type protein by circular dichroism spectroscopy.

Steady-state and adenylation kinetics

The single substrate steady-state kinetics of *bs*MenE and its mutants was determined as described previously (22, 24, 26). The assay was coupled to excessive MenB obtained from previous studies (35–37), which converts the *bs*MenE product OSB-CoA to DHNA-CoA for measurement of the DHNA-CoA characteristic absorbance at 392 nm (molar extinction coefficient $\epsilon = 4000\ \text{M}^{-1}\cdot\text{cm}^{-1}$) (38). The substrate OSB was chemoenzymatically prepared from chorismate using the enzymes EntC, MenC, MenD, and MenH obtained from previous studies (39–45) and purified by reverse-phase HPLC. Chorismate was prepared from an engineered bacterial strain as described previously (46).

The single-turnover adenylation half-reaction rate was determined using a previously described method with minor modifications (22). The assay was carried out in the presence of OSB and ATP without coenzyme A, and its rate was determined by coupling to inorganic pyrophosphatase (IPP) and purine nucleoside phosphorylase (PNP) (47), which hydrolyze the pyrophosphate product to phosphate and convert phosphate into 2-amino-6-mercapto-7-methylpurine ($\epsilon = 11{,}000\ \text{M}^{-1}\cdot\text{cm}^{-1}$ at 360 nm) in the presence of 2-amino-6-mercapto-7-methylpurine ribonucleoside (MESG), respectively (23). A typical reaction contained 1 mM OSB, 1 mM ATP, 0.2 unit of PNP, 0.08 unit of IPP, 400 μM MESG, 10 mM $MgCl_2$, and 20 mM NaCl in 50 mM Tris-HCl (pH 7.5) and was initiated by addition of 10 μM wild-type *bs*MenE or its mutants after a 1-min incubation. The slopes of the initial linear region of the progress curves were used to calculate the initial reaction rates, which were normalized by setting the rate of the wild-type *bs*MenE to 100%. All the assays were repeated three times at 20 °C.

Chemoenzymatic synthesis of OSB-NCoA

OSB-NCoA was synthesized as an analogue of the OSB-CoA product of the *bs*MenE-catalyzed reaction using a previously reported chemoenzymatic method (27, 48, 49). First, OSB-amino-pantetheine was synthesized following the reported procedure (27) from 2-acetylbenzoic acid, calcium D-pantothenate, 2-bromoethylamine hydrobromide, and glyoxylic acid that were bought from Tokyo Chemical Industry. Subsequently, this precursor was chemoenzymatically converted into OSB-NCoA using the enzymes PanK, PPAT, and dephosphocoenzyme A kinase, as described previously (48, 49), and purified by HPLC. Identity of OSB-NCoA was confirmed by electrospray ionization mass spectrometry (ESI-MS) with the molecular ions at 953.3 $[M - H]^-$ and 476.2 $[M - 2H]^{2-}$, which are consistent with its calculated mass of 954.6 (molecular formula: $C_{32}H_{45}N_8O_{20}P_3$). OSB-NCoA concentration was determined by its absorbance at 260 nm with the extinction coefficient ϵ of 15,000 $\text{m}^{-1}\ \text{cm}^{-1}$. We thank Professor Gerard Wright in Department of Biochemistry, McMaster University for the generous gifts of plasmids for overexpression and purification of PanK, PPAT, and dpCoAK hexahistidine-tagged proteins (48).

Crystallization, data collection, structure determination, and refinement

The initial crystallization screen was carried out for the wild-type non-tagged *bs*MenE at 10, 15, and 20 mg/ml supplemented with 3 mM OSB-NCoA and 20 mM $MgCl_2$, mixed with the reservoir solution at a 1:1 ratio, and subjected to sitting drop vapor diffusion at 16 °C using commercial kits from Hampton Research (Index, Crystal Screen, and PEG-Rx), Rigaku (Wizard 3&4), and Molecular Dimension (JCSG1&2). Small bar-shaped crystals were observed in one condition (#21, Wizard 4) after 3 days. The crystals were easily reproduced in optimization experiments and grown to a size of ~300 μm in the longest dimension in subsequent additive screening. The resulting crystals diffracted to a high resolution of ~1.7 Å, but each diffraction point was severely split, giving rise to uninterpretable diffraction datasets obtained from either in-house diffractometers or synchrotron radiation facilities. This twinning problem remained after seeding, optimization of cryoprotectants, or additional additive screenings at multiple temperatures (8, 12, 16, and 20 °C).

Crystallization screens for the double mutant I454R/A456K (IRAK) of *bs*MenE were conducted using essentially the same protocol as for the wild-type protein. In a parallel screen, 0.8 mM AMP was added to the protein solution to capture a ternary complex. Several rectangular single crystals were observed within 3 days in a JCSG condition (JCSG1 #46) containing 40% v/v PEG300, 0.1 M sodium cacodylate (pH 6.5), and 0.2 M calcium acetate. Further optimization gave rise to more regular cubic/rectangular crystals using the reservoir solution of 32% v/v PEG300 containing 0.15 M sodium cacodylate (pH 6.5) and 0.2 M calcium acetate. In-house tests showed excellent diffraction quality and low mosaicity in a *P*1 space group for the crystals of both the binary (IRAK–OSB-NCoA) and ternary (IRAK–OSB-NCoA–AMP) complexes, which were grown under the same conditions.

X-ray diffraction data were collected at 100 K for the two *bs*MenE complexes at BL17U with an ADSC Quantum 315R charge-coupled device detector at the Shanghai Synchrotron Radiation Facility (SSRF) (50) or BL19U1 with a PILATUS3 6M detector at the National Facility for Protein Science Shanghai, China. To achieve high completeness and redundancy for the ternary complex crystal in the *P*1 space group, 720 diffraction frames were collected with the oscillation angle set at 0.5° per frame and the Φ angle rotated from 0 to 360°. All the images were indexed, integrated by iMosflm (51), and scaled by Aimless (52) in the CCP4 Suite. The highest resolution was set to 1.76 Å, and its Matthews coefficient indicated four protein molecules in the unit cell (53). For the binary complex, 440 diffraction frames were collected where the oscillation angle was set to 1.0° per frame and the Φ angle rotated from 0 to 440°, and the images were similarly processed as for the ternary complex. The statistics of data collection and processing are summarized in Table 2.

The ternary structure was solved by molecular replacement (MR) by Phaser-MR in PHENIX (54), where the N-domain (residues 1–379) of the ligand-free *bs*MenE structure (PDB code 5BUQ, chain A) was used as search model. The unit cell contained four homologous subunits that were nicely fitted to the initial electron density map as checked in COOT (55). Rigid-body refinement was performed by PHENIX-Refine (56) with 5% reflection taken for R_{free} calculation. The resulting R_{work}/R_{free} reduced from 0.4042/0.4040 to 0.3122/0.3470, indicating a correct MR solution. After the preliminary refinement, the C-domain of chain A was built manually by COOT based on the extra electron density, and non-crystal symmetry was applied to generate the C-domains of the other three subunits. Subsequently, the coordinates and geometry constraints of the two ligand molecules were prepared by eLBOW (57). OSB-NCoA was unambiguously modeled to the extra density at the inter-domain channel of all four subunits, although we could only observe a relatively poor density for AMP in chain A and chain C. As the refinement converged, TLS anisotropic refinement was incorporated in which each subunit was partitioned into four segments (residues 1–162, 163–305, 306–381, and 382–486) as analyzed by TLSMD (58). Chain C of the finalized ternary structure was used as the MR template to solve the binary structure (IRAK-OSB-NCoA), which was refined and examined with the same procedure as the ternary structure. The overall data quality was assessed by PROCHECK (59) and MolProbity (60). The statistics for the structural refinement are given in Table 2.

Structural analysis and sequence alignment

All graphics were generated by PyMOL (61), which was also used to perform structural analysis of the protein crystal structures. The C-domain rotation angle and the involved bending residues were calculated by the DynDom server (29). The interfaces were analyzed; and the quaternary structure was determined using PISA (28), and the electrostatic potential surface was calculated using PDB2PQR plus APBS (62). Multiple sequence alignment was performed with ClustalW 2.0 (63) or Clustal Omega (64) for structure-based presentation using ESPript 3.0 (25).

Author contributions—Z. G. conceived and coordinated the study. Z. G. and Y. C. wrote the paper. Y. C. designed, performed, and analyzed the experiments in all figures. Y. C. and L. T. L. participated in protein purification, protein crystallization, data collection, and structural determination. Y. C., L. T. L., X. B. L., X. L., and X. D. L. carried out the chemoenzymatic synthesis of the product analogue and prepared all relevant enzymes. All authors reviewed the results and approved the final version of the manuscript.

Acknowledgments—We thank the staffs from beamline BL17U1 of Shanghai Synchrotron Radiation Facility (SSRF) and beamline BL19U1 of National Facility for Protein Science Shanghai, China, for on-site technical assistance during data collection.

References

1. Akerley, B. J., Rubin, E. J., Novick, V. L., Amaya, K., Judson, N., and Mekalanos, J. J. (2002) A genome-scale analysis for identification of genes required for growth or survival of *Haemophilus influenzae*. *Proc. Natl. Acad. Sci. U.S.A.* **99,** 966–971
2. Forsyth, R. A., Haselbeck, R. J., Ohlsen, K. L., Yamamoto, R. T., Xu, H., Trawick, J. D., Wall, D., Wang, L., Vickie, B. D., Froelich, J. M., Kedar, G. C., King, P., McCarthy, M., Malone, C., Misiner, B., *et al.* (2002) A genome-wide strategy for the identification of essential genes in *Staphylococcus aureus*. *Mol. Microbiol.* **43,** 1387–1400
3. Kobayashi, K., Ehrlich, S. D., Albertini, A., Amati, G., Andersen, K. K., Arnaud, M., Asai, K., Ashikaga, S., Aymerich, S., Bessieres, P., Boland, F., Brignell, S. C., Bron, S., Bunai, K., Chapuis, J., *et al.* (2003) Essential *Bacillus subtilis* genes. *Proc. Natl. Acad. Sci. U.S.A.* **100,** 4678–4683
4. Kurosu, M., Narayanasamy, P., Biswas, K., Dhiman, R., and Crick, D. C. (2007) Discovery of 1,4-dihydroxy-2-naphthoate prenyltransferase inhibitors: new drug leads for multidrug-resistant Gram-positive pathogens. *J. Med. Chem.* **50,** 3973–3975
5. Lu, X., Zhang, H., Tonge, P. J., and Tan, D. S. (2008) Mechanism-based inhibitors of MenE, an acyl-CoA synthetase involved in bacterial menaquinone biosynthesis. *Bioorg. Med. Chem. Lett.* **18,** 5963–5966
6. Dhiman, R. K., Mahapatra, S., Slayden, R. A., Boyne, M. E., Lenaerts, A., Hinshaw, J. C., Angala, S. K., Chatterjee, D., Biswas, K., Narayanasamy, P., Kurosu, M., and Crick, D. C. (2009) Menaquinone synthesis is critical for maintaining mycobacterial viability during exponential growth and recovery from non-replicating persistence. *Mol. Microbiol.* **72,** 85–97
7. Gulick, A. M. (2009) Conformational dynamics in the acyl-CoA synthetases, adenylation domains of nonribosomal peptide synthetases, and firefly luciferase. *ACS Chem. Biol.* **4,** 811–827
8. Gulick, A. M., Starai, V. J., Horswill, A. R., Homick, K. M., and Escalante-Semerena, J. C. (2003) The 1.75 Å crystal structure of acetyl-CoA synthetase bound to adenosine-5′-propylphosphate and coenzyme A. *Biochemistry* **42,** 2866–2873
9. Reger, A. S., Wu, R., Dunaway-Mariano, D., and Gulick, A. M. (2008) Structural characterization of a 140° domain movement in the two-step reaction catalyzed by 4-chlorobenzoate:CoA ligase. *Biochemistry* **47,** 8016–8025
10. Wu, R., Cao, J., Lu, X., Reger, A. S., Gulick, A. M., and Dunaway-Mariano, D. (2008) Mechanism of 4-chlorobenzoate:coenzyme A ligase catalysis. *Biochemistry* **47,** 8026–8039
11. Reger, A. S., Carney, J. M., and Gulick, A. M. (2007) Biochemical and crystallographic analysis of substrate binding and conformational changes in acetyl-CoA synthetase. *Biochemistry* **46,** 6536–6546
12. Branchini, B. R., Southworth, T. L., Murtiashaw, M. H., Wilkinson, S. R., Khattak, N. F., Rosenberg, J. C., and Zimmer, M. (2005) Mutagenesis evidence that the partial reactions of firefly bioluminescence are catalyzed by different conformations of the luciferase C-terminal domain. *Biochemistry* **44,** 1385–1393
13. Drake, E. J., Nicolai, D. A., and Gulick, A. M. (2006) Structure of the EntB multidomain nonribosomal peptide synthetase and functional analysis of its interaction with the EntE adenylation domain. *Chem. Biol.* **13,** 409–419
14. Gulick, A. M., Lu, X., and Dunaway-Mariano, D. (2004) Crystal structure of 4-chlorobenzoate:CoA ligase/synthetase in the unliganded and aryl substrate-bound states, *Biochemistry* **43,** 8670–8679
15. Conti, E., Franks, N. P., and Brick, P. (1996) Crystal structure of firefly luciferase throws light on a superfamily of adenylate-forming enzymes. *Structure* **4,** 287–298
16. Sundlov, J. A., Fontaine, D. M., Southworth, T. L., Branchini, B. R., and Gulick, A. M. (2012) Crystal structure of firefly luciferase in a second catalytic conformation supports a domain alternation mechanism. *Biochemistry* **51,** 6493–6495
17. Yonus, H., Neumann, P., Zimmermann, S., May, J. J., Marahiel, M. A., and Stubbs, M. T. (2008) Crystal structure of DltA. Implications for the reaction mechanism of non-ribosomal peptide synthetase adenylation domains. *J. Biol. Chem.* **283,** 32484–32491
18. Du, L., He, Y., and Luo, Y. (2008) Crystal structure and enantiomer selection by D-alanyl carrier protein ligase DltA from *Bacillus cereus*. *Biochemistry* **47,** 11473–11480
19. Kochan, G., Pilka, E. S., von Delft, F., Oppermann, U., and Yue, W. W. (2009) Structural snapshots for the conformation-dependent catalysis by

human medium-chain acyl-coenzyme A synthetase ACSM2A. *J. Mol. Biol.* **388,** 997–1008
20. Li, Z., and Nair, S. K. (2015) Structural basis for specificity and flexibility in a plant 4-coumarate:CoA ligase. *Structure* **23,** 2032–2042
21. Lu, X., Zhou, R., Sharma, I., Li, X., Kumar, G., Swaminathan, S., Tonge, P. J., and Tan, D. S. (2012) Stable analogues of OSB-AMP: potent inhibitors of MenE, the *o*-succinylbenzoate-CoA synthetase from bacterial menaquinone biosynthesis. *ChemBioChem* **13,** 129–136
22. Tian, Y., Suk, D.-H., Cai, F., Crich, D., and Mesecar, A. D. (2008) *Bacillus anthracis o*-succinylbenzoyl-CoA synthetase: reaction kinetics and a novel inhibitor mimicking its reaction intermediate. *Biochemistry* **47,** 12434–12447
23. Tian, Y. (2008) *The Reaction Kinetics, Crystal Structures and Novel Inhibitors of Bacterial OSB-CoA Synthetase*. Ph.D. thesis, University of Illinois at Chicago
24. Chen, Y., Sun, Y., Song, H., and Guo, Z. (2015) Structural basis for the ATP-dependent configuration of adenylation active site in *Bacillus subtilis o*-succinylbenzoyl-CoA synthetase. *J. Biol. Chem.* **290,** 23971–23983
25. Robert, X., and Gouet, P. (2014) Deciphering key features in protein structures with the new ENDscript server. *Nucleic Acids Res.* **42,** W320–W324
26. Chen, Y., Jiang, Y., and Guo, Z. (2016) Mechanistic insights from the crystal structure of *Bacillus subtilis o*-succinylbenzoyl-CoA synthetase complexed with the adenylate intermediate. *Biochemistry* **55,** 6685–6695
27. Li, H. J., Li, X., Liu, N., Zhang, H., Truglio, J. J., Mishra, S., Kisker, C., Garcia-Diaz, M., and Tonge, P. J. (2011) Mechanism of the intramolecular Claisen condensation reaction catalyzed by MenB, a crotonase superfamily member. *Biochemistry* **50,** 9532–9544
28. Krissinel, E., and Henrick, K. (2007) Inference of macromolecular assemblies from crystalline state. *J. Mol. Biol.* **372,** 774–797
29. Taylor, D., Cawley, G., and Hayward, S. (2014) Quantitative method for the assignment of hinge and shear mechanism in protein domain movements. *Bioinformatics* **30,** 3189–3196
30. The UniProt Consortium (2017) UniProt: the universal protein knowledgebase. *Nucleic Acids Res.* **45,** D158–D169
31. Sillitoe, I., Lewis, T. E., Cuff, A., Das, S., Ashford, P., Dawson, N. L., Furnham, N., Laskowski, R. A., Lee, D., Lees, J. G., Lehtinen, S., Studer, R. A., Thornton, J., and Orengo, C. A. (2015) CATH: comprehensive structural and functional annotations for genome sequences. *Nucleic Acids Res.* **43,** D376–D381
32. Khare, G., Gupta, V., Gupta, R. K., Gupta, R., Bhat, R., and Tyagi, A. K. (2009) Dissecting the role of critical residues and substrate preference of a fatty acyl-CoA synthetase (FadD13) of *Mycobacterium tuberculosis*. *PLoS ONE* **4,** E8387–E8387
33. Kim, H. U., van Oostende, C., Basset, G. J., and Browse, J. (2008) The AAE14 gene encodes the *Arabidopsis o*-succinylbenzoyl-CoA ligase that is essential for phylloquinone synthesis and photosystem-I function. *Plant J.* **54,** 272–283
34. Law, A., and Boulanger, M. J. (2011) Defining a structural and kinetic rationale for paralogous copies of phenylacetate-CoA ligases from the cystic fibrosis pathogen *Burkholderia cenocepacia* J2315. *J. Biol. Chem.* **286,** 15577–15585
35. Jiang, M., Chen, M., Guo, Z. F., and Guo, Z. (2010) A bicarbonate cofactor modulates 1,4-dihydroxy-2-naphthoyl coenzyme A synthase in menaquinone biosynthesis of *Escherichia coli*. *J. Biol. Chem.* **285,** 30159–30169
36. Sun, Y., Song, H., Li, J., Jiang, M., Li, Y., Zhou, J., and Guo, Z. (2012) Active site binding and catalytic role of bicarbonate in 1,4-dihydroxy-2-naphthoyl coenzyme A synthases from vitamin K biosynthetic pathways. *Biochemistry* **51,** 4580–4589
37. Song, H., Sung, H. P., Tse, Y. S., Jiang, M., and Guo, Z. (2014) Ligand-dependent active site closure revealed in the crystal structure of *Mycobacterium tuberculosis* MenB complexed with product analogues. *Acta Crystallogr. D Biol. Crystallogr.* **70,** 2959–2969
38. Chen, M., Jiang, M., Sun, Y., Guo, Z. F., and Guo, Z. (2011) Stabilization of the second oxyanion intermediate by 1,4-dihydroxy-2-naphthoyl coenzyme A synthase of the menaquinone pathway: spectroscopic evidence of the involvement of a conserved aspartic acid. *Biochemistry* **50,** 5893–5904
39. Jiang, M., and Guo, Z. (2007) Effects of macromolecular crowding on the intrinsic catalytic efficiency and structure of enterobactin-specific isochorismate synthase. *J. Am. Chem. Soc.* **129,** 730–731
40. Jiang, M., Cao, Y., Guo, Z.-F., Chen, M., Chen, X., and Guo, Z. (2007) Menaquinone biosynthesis in *Escherichia coli*: identification of 2-succinyl-5-enolpyruvyl-6-hydroxyl-3-cyclohexene-1-carboxylate (SEPHCHC) as a novel intermediate and re-evaluation of MenD activity. *Biochemistry* **46,** 10979–10989
41. Jiang, M., Chen, M., Cao, Y., Yang, Y., Sze, K. H., Chen, X., and Guo, Z. (2007) Determination of the stereochemistry of 2-succinyl-5-enolpyruvyl-6-hydroxy-3-cyclohexene-1-carboxylic acid, a key intermediate in menaquinone biosynthesis. *Org. Lett.* **9,** 4765–4767
42. Song, H., Dong, C., Qin, M., Chen, Y., Sun, Y., Liu, J., Chan, W., and Guo, Z. (2016) A thiamine-dependent enzyme utilizes an active tetrahedral intermediate in vitamin K biosynthesis. *J. Am. Chem. Soc.* **138,** 7244–7247
43. Jiang, M., Chen, X., Guo, Z.-F., Cao, Y., Chen, M., and Guo, Z. (2008) Identification and characterization of (1*R*,6*R*)-2-succinyl-6-hydroxy-2,4-cyclohexadiene-1-carboxylate synthase in the menaquinone biosynthesis of. *Escherichia coli*. *Biochemistry* **47,** 3426–3434
44. Jiang, M., Chen, X., Wu, X. H., Chen, M., Wu, Y. D., and Guo, Z. (2009) Catalytic mechanism of SHCHC synthase in the menaquinone biosynthesis of *Escherichia coli*: identification and mutational analysis of the active-site residues. *Biochemistry* **48,** 6921–6931
45. Sun, Y., Yin, S., Feng, Y., Li, J., Zhou, J., Liu, C., Zhu, G., and Guo, Z. (2014) Molecular basis of the general base catalysis of an α/β-hydrolase catalytic triad. *J. Biol. Chem.* **289,** 15867–15879
46. Grisostomi, G., Kast, P., Pulido, R., Huynh, J., and Hilvert, D. (1997) Efficient *in vivo* synthesis and rapid purification of chorismic acid using an engineered *Escherichia coli* strain. *Bioorg. Chem.* **25,** 297–305
47. Webb, M. R. (1992) A continuous spectrophotometric assay for inorganic-phosphate and for measuring phosphate release kinetics in biological systems. *Proc. Natl. Acad. Sci. U.S.A.* **89,** 4884–4887
48. Nazi, I., Koteva, K. P., and Wright, G. D. (2004) One-pot chemoenzymatic preparation of coenzyme A analogues. *Anal. Biochem.* **324,** 100–105
49. van Wyk, M., and Strauss, E. (2007) One-pot preparation of coenzyme A analogues via an improved chemoenzymatic synthesis of pre-CoA thioester synthons. *Chem. Commun.* **2007,** 398–400
50. Wang, Q.-S., Yu, F., Huang, S., Sun, B., Zhang, K.-H., Liu, K., Wang, Z.-J., Xu C-y Wang. S-S, Yang, L.-F., Pan, Q.-Y., Li, L., Zhou, H., Cui, Y., Xu, Q., Earnest, T., and He, J.-H. (2015) The macromolecular crystallography beamline of SSRF. *Nuclear Sci. Tech.* **26,** 010102
51. Battye, T. G., Kontogiannis, L., Johnson, O., Powell, H. R., and Leslie, A. G. (2011) iMOSFLM: a new graphical interface for diffraction-image processing with MOSFLM. *Acta Crystallogr. D Biol. Crystallogr.* **67,** 271–281
52. Evans, P. R., and Murshudov, G. N. (2013) How good are my data and what is the resolution? *Acta Crystallogr. D Biol. Crystallogr.* **69,** 1204–1214
53. Kantardjieff, K. A., and Rupp, B. (2003) Matthews coefficient probabilities: improved estimates for unit cell contents of proteins, DNA, and protein-nucleic acid complex crystals. *Protein Sci.* **12,** 1865–1871
54. Adams, P. D., Afonine, P. V., Bunkóczi, G., Chen, V. B., Davis, I. W., Echols, N., Headd, J. J., Hung, L. W., Kapral, G. J., Grosse-Kunstleve, R. W., McCoy, A. J., Moriarty, N. W., Oeffner, R., Read, R. J., Richardson, D. C., *et al.* (2010) PHENIX: a comprehensive Python-based system for macromolecular structure solution. *Acta Crystallogr. D Biol. Crystallogr.* **66,** 213–221
55. Emsley, P., Lohkamp, B., Scott, W. G., and Cowtan, K. (2010) Features and development of Coot. *Acta Crystallogr. D Biol. Crystallogr.* **66,** 486–501
56. Echols, N., Moriarty, N. W., Klei, H. E., Afonine, P. V., Bunkóczi, G., Headd, J. J., McCoy, A. J., Oeffner, R. D., Read, R. J., Terwilliger, T. C., and Adams, P. D. (2014) Automating crystallographic structure solution and refinement of protein-ligand complexes. *Acta Crystallogr. D Biol. Crystallogr.* **70,** 144–154
57. Moriarty, N. W., Grosse-Kunstleve, R. W., and Adams, P. D. (2009) Electronic ligand builder and optimization workbench (eLBOW): a tool for ligand coordinate and restraint generation. *Acta Crystallogr. D Biol. Crystallogr.* **65,** 1074–1080
58. Winn, M. D., Isupov, M. N., and Murshudov, G. N. (2001) Use of TLS parameters to model anisotropic displacements in macromolecular refinement. *Acta Crystallogr. D Biol. Crystallogr.* **57,** 122–133

59. Laskowski, R. A., Macarthur, M. W., Moss, D. S., and Thornton, J. M. (1993) Procheck–a program to check the stereochemical quality of protein structures. *J. Appl. Crystallogr.* **26,** 283–291
60. Chen, V. B., Arendall, W. B., 3rd., Headd, J. J., Keedy, D. A., Immormino, R. M., Kapral, G. J., Murray, L. W., Richardson, J. S., and Richardson, D. C. (2010) MolProbity: all-atom structure validation for macromolecular crystallography. *Acta Crystallogr. D Biol. Crystallogr.* **66,** 12–21
61. DeLano, W. L. (2002) *The PyMOL Molecular Graphics System.* Version 1.3, DeLano Scientific, San Carlos, CA
62. Dolinsky, T. J., Nielsen, J. E., McCammon, J. A., and Baker, N. A. (2004) PDB2PQR: an automated pipeline for the setup, execution, and analysis of Poisson-Boltzmann electrostatics calculations. *Nucleic Acids Res.* **32,** W665–W667
63. Larkin, M. A., Blackshields, G., Brown, N. P., Chenna, R., McGettigan, P. A., McWilliam, H., Valentin, F., Wallace, I. M., Wilm, A., Lopez, R., Thompson, J. D., Gibson, T. J., and Higgins, D. G. (2007) Clustal W and Clustal X, Version 2.0. *Bioinformatics* **23,** 2947–2948
64. Sievers, F., Wilm, A., Dineen, D., Gibson, T. J., Karplus, K., Li, W., Lopez, R., McWilliam, H., Remmert, M., Söding, J., Thompson, J. D., and Higgins, D. G. (2011) Fast, scalable generation of high-quality protein multiple sequence alignments using Clustal Omega. *Mol. Syst. Biol.* **7,** 539

Crystal structure of the thioesterification conformation of *Bacillus subtilis o*-succinylbenzoyl-CoA synthetase reveals a distinct substrate-binding mode

Yaozong Chen, Tin Lok Li, Xingbang Lin, Xin Li, Xiang David Li and Zhihong Guo

J. Biol. Chem. 2017, 292:12296-12310.
doi: 10.1074/jbc.M117.790410 originally published online May 30, 2017